

# Nanoscale

Accepted Manuscript



This is an *Accepted Manuscript*, which has been through the Royal Society of Chemistry peer review process and has been accepted for publication.

*Accepted Manuscripts* are published online shortly after acceptance, before technical editing, formatting and proof reading. Using this free service, authors can make their results available to the community, in citable form, before we publish the edited article. We will replace this *Accepted Manuscript* with the edited and formatted *Advance Article* as soon as it is available.

You can find more information about *Accepted Manuscripts* in the [Information for Authors](#).

Please note that technical editing may introduce minor changes to the text and/or graphics, which may alter content. The journal's standard [Terms & Conditions](#) and the [Ethical guidelines](#) still apply. In no event shall the Royal Society of Chemistry be held responsible for any errors or omissions in this *Accepted Manuscript* or any consequences arising from the use of any information it contains.



### 3D nanostructures fabricated by advanced stencil lithography

F. Yesilkoy,<sup>a,b</sup> V. Flauraud,<sup>a</sup> M. Rüegg,<sup>a</sup> B.J. Kim<sup>b</sup> and J. Brugger<sup>a\*\*†</sup>

Received 28th November 2015,  
Accepted 24th January 2016

DOI: 10.1039/x0xx00000x

[www.rsc.org/](http://www.rsc.org/)

**This letter reports on a novel fabrication method of 3D metal nanostructures using high-throughput nanostencil lithography. Aperture clogging, which occurs on the stencil membranes during physical vapor deposition, is leveraged to create complex topographies in nanoscale. Precision of the 3D nanofabrication method is studied in terms of geometric parameters and material types. The versatility of the technique is demonstrated on various symmetric and chiral patterns made of Al and Au.**

Recent efforts in advancing nanofabrication techniques towards control over three dimensions (3D) in the nanoscale have promoted promising new fields of research. For instance, metal nanostructures with chiral properties, which require 3D features, have been highlighted in many recent reports for their potential in enhancing optical enantiomer sensing, with a particular focus on label-free and ultrasensitive detection of biomolecules using circular dichroism spectroscopy.<sup>1,2</sup> Moreover, 3D structured surfaces with arrayed non-planar metamolecules have been demonstrated to act as tunable polarization modulators in infrared and longer wavelengths, leading to the development of photonic circuits and new photonic devices.<sup>3–5</sup> In the field of SERS, 3D hybrid material (Au-SiO<sub>2</sub>-Au) nanocones<sup>6</sup> and flower-like metal geometries<sup>7</sup> have been reported to enhance sensitivity and to tune the resonant frequency of SERS measurements. Likewise, a 3D version of the well-known bow-tie nanoantennas has been reported to show extraordinary absorption properties.<sup>8</sup> Another blossoming research field that benefits from 3D nanofabrication is that of bio-inspired artificial smart surfaces, which aims to mimic 3D micro/nanostructures found in nature to engineer superhydrophobic,<sup>9–11</sup> anti-glare,<sup>10</sup> anti-reflective,<sup>10,11</sup> and anti-bacterial surfaces.<sup>12</sup> The future of these applications relies on key advancements that will enable high-throughput, large area, cost-effective and versatile

nanofabrication technologies with precise control over the third dimension.

The current state-of-the-art in nanotechnology is the culmination of the parallel development of fabrication methods in two major branches: top-down, namely lithographic techniques; and bottom-up, such as molecular self-assembly techniques. Experts in both fields are making inroads in adapting the current technology to develop nanoscale control for 3D nanofabrication. Among the top-down methods, the following three have been successfully employed to create a variety of 3D nano geometries: multistep Electron Beam Lithography (EBL),<sup>13</sup> direct laser writing combined with EBL<sup>14</sup> or metal plating,<sup>15</sup> and focused ion/electron beam induced deposition<sup>16</sup> or milling.<sup>17</sup> While these serial focused beam methods offer nanoscale precision both locally on the individual structures and globally in their spatial distribution, they are not high-throughput, which makes large-area applications very expensive. On the other hand, self-assembly techniques, particularly DNA origami,<sup>18,19</sup> allow for versatile 3D geometry formations using metal nanoparticles as building blocks. However, the homogeneous synthesis of metal nanoparticles requires intricate chemistry, and the wide-range spatial ordering of the synthesized 3D structures is not straightforward.<sup>20</sup> Further hybrid achievements in 3D nanofabrication were made using colloidal lithography combined with oblique UV exposure for the fabrication of hollow-core structures made of photosensitive polymers.<sup>21</sup> Moreover, colloidal lithography was used together with oblique metal deposition or etching for the fabrication of spiral-like metal chiral structures<sup>22</sup> and tunable perfect absorber surfaces.<sup>23</sup> While these methods benefit from the low-cost and high-throughput nature of the colloidal lithography, they do not offer versatility in geometry neither are straightforward to fabricate without dedicated add-on tools to conventional fabrication equipment. Therefore, there is still a pressing need for a high-throughput and large-area 3D nanofabrication method, which can be implemented using standard lithography equipment, and offers material/substrate flexibility and geometry versatility.

<sup>a</sup> EPFL STI IMT LMIS1, CH-1015 Lausanne Switzerland.

<sup>\*</sup> Corresponding Author E-mail: [juergen.brugger@epfl.ch](mailto:juergen.brugger@epfl.ch)

<sup>b</sup> The University of Tokyo IIS CIRMM, 4-6-1 Komaba, Meguro-ku, Tokyo 153-8505, Japan.

<sup>†</sup> F.Y. and J.B. conceived the study; V.F. fabricated the stencil masks; F.Y. fabricated the nanostructures; F.Y. and M.R. collected and analysed data; F.Y., M.R. and J.B. wrote the manuscript; V.F. and B.J.K. gave technical support and conceptual advice.

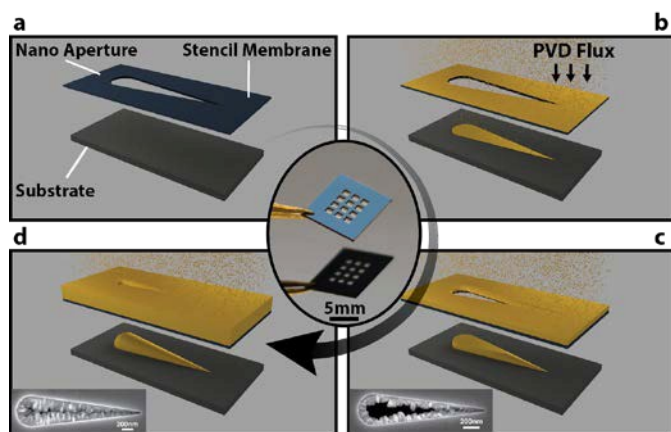


**Figure 1.** Stencil lithography clogging effect. a) Pre-deposition phase: stencil mask is assembled on a substrate using Kapton® tape. Three representative phases of stencil aperture clogging are shown clockwise: b) Initial Phase: PVD occurs through the fully open aperture. c) Intermediate Phase: aperture is partially clogged. d) Final phase: Aperture is fully clogged and final 3D nanostructure with non-uniform height is formed. Inlets show the SEM images of the apertures on the stencil membranes, taken from the substrate-facing side after Al deposition. The center picture shows a stencil mask chip of 10 mm X 12 mm with twelve membranes, each of 1 mm<sup>2</sup> area.

In this work, we demonstrate the use of nanostencil lithography for the facile fabrication of 3D metal nanostructures that features complex non-uniform thickness profiles delimited by the aperture pattern on the stencil mask. Stencil lithography, or shadow masking, is a resistless lithography technique that offers both additive and subtractive patterning in a wide dimension scale (milli-nano).<sup>24</sup> Moreover, it distinguishes itself from the other nanofabrication techniques by its well-known advantages, such as straightforward fabrication, substrate independence, lack of high-temperature and wet chemical process steps, wafer-scale high throughput and cost effectiveness due to the reusability of the mask once they are cleaned.<sup>25</sup> Our method relies on aperture clogging, which naturally occurs on the stencil membrane during material deposition, and leads to lateral pattern shrinkage, projecting 2D patterns as 3D nanostructures on the target substrate. Leveraging the nanometric precision and geometric versatility of EBL, which is used to fabricate two-dimensional apertures on the stencil membranes, we scrutinize the aperture width regulated inhomogeneous thickness control on individual metal nanostructures. Figure 1 describes the proposed technique by illustrating representative phases of material deposition through a stencil membrane and the resulting 3D structure at each phase. SEM micrographs taken from the substrate-facing side of partially and fully clogged stencils during the Al deposition process are shown as inset images in Figure 1.

The nanostencil masks used in this work contain twelve low-stress silicon nitride (LS-SiN) membranes that are 100 nm thick and 1 mm<sup>2</sup> in area. The nano-sized geometric patterns were transferred onto the membranes using EBL and the apertures were etched using dry etching. The stencil membranes are supported by 10 mm x 12 mm Si-chips (Figure 1 center). Detailed information on the fabrication of the nanostencil masks is reported elsewhere.<sup>26</sup> The metal deposition was

performed using Physical Vapor Deposition (PVD) technique under vacuum (10<sup>-5</sup> torr) at average 3 Å/s and 5 Å/s deposition rates for Cr/Au and Al, respectively, on Si chips at room temperature. The nanostencil masks were assembled on Si-substrates and temporarily secured with Kapton® adhesive tape before the metal deposition. The inherent gap between the mask membrane and the substrate, which has been previously characterized to be in 1 μm range,<sup>27</sup> was sufficient for our pattern dimension scale. However, it can be controlled using spacers for the structures with higher aspect ratios.

The stencil aperture-clogging rate is a critical parameter in the design of the final 3D geometry. In order to quantify the clogging effect on the topography of the 3D metal nanostructures, we used a geometric shape with varying width, which we call “tapered line” identified by its maximum width (W) and total length (L) (Figure 2 a). Figure 2 b depicts SEM micrographs of an Al tapered line and its corresponding stencil mask (W/L = 0.5 μm / 1.25 μm) after a 500 nm deposition that achieved full clogging. Figure 2 c shows an AFM image of the same geometry, which reveals—as expected—that these structures exhibit non-uniform elevation. The AFM data, which was acquired using JSPM 5200 Scanning Probe Microscopy unit operated in the tapping mode, was used to derive the relationship between the aperture clogging and height of the structures.

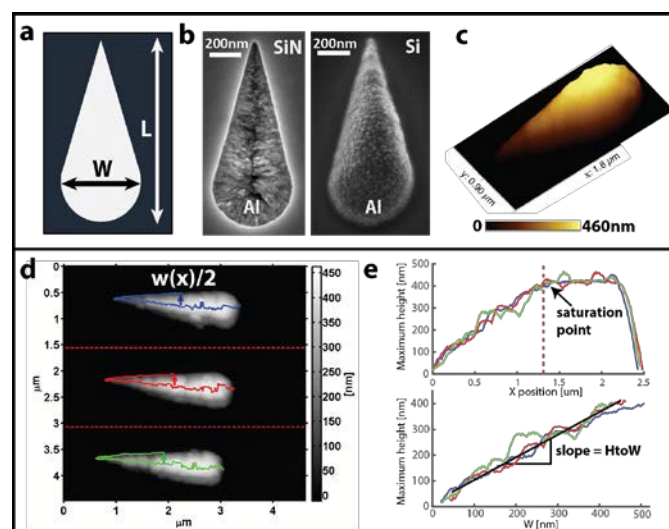


**Figure 2.** Width to height ratio characterization on tapered line geometry. Top row describes the tapered geometry: a) Tapered geometry is defined by its total length (L) and maximum width (W). b) SEM tilted (20°) image of a tapered structure (W/L=0.5 μm/1 μm) formed by depositing 500 nm of Al on Si-substrate (right) and its corresponding fully clogged stencil mask after deposition (left). c) 3D AFM topography of the structure. Bottom row describes the analysis performed on the AFM topography data to extract relation between the aperture width and the maximum height achieved: d) Maximum height point and half-width associated with that point is identified on the vertical lines of each tapered geometry. e) Maximum height profile plots (top), where height saturation point is determined (red dashed line) and non-saturated part of the maximum height profile associated with the width of the structure measured on the same vertical line re-plotted (bottom). The HtoW ratio is extracted from the slope of the linearly fitted data.

For semi-automated characterization of the height profiles, an algorithm in MATLAB was developed to process the AFM topographical data. The algorithm identifies an individual tapered structure, extracts the maximum height values along its longitudinal axis and associates each value with the width of the structure measured along the perpendicular line intersecting the maximum point. Figure 2 d visually describes the output of this computational analysis, where the dashed lines separate each structure in a single AFM scan area, and the maximum height at each point is associated with its corresponding half-width. Next, we manually located the saturation point where the clogging stops and the structure levels out (Figure 2 e), which occurs when the total amount of material deposited (400 nm in this case) is not enough to achieve full clogging of the aperture. In what follows, only the region of the structures before the saturation point is considered in order to eliminate the effect of the total deposited metal thickness. Finally, we plotted the height variation as a function of the width (Figure 2 e). Fitting the data to a first-degree polynomial and we extracted the height to width (HtoW) ratio, which is used to quantify the clogging rate.

The HtoW ratio over three different tapered line geometries ( $W=300, 400, 500$  nm and  $L=2$   $\mu\text{m}$ ) were measured for both 400 nm Al and Au depositions. We analyzed twelve different tapered line structures of each kind from different locations on the chip, and averaged the computed HtoW ratio (Figure 3). Our results show that the clogging rate does not depend significantly on the geometric parameters of the aperture. However, we observed that the HtoW ratio for different materials, namely Al and Au, are significantly different, regardless of the stencil geometry. The average HtoW ratio is measured to be 1.69 for Au and 0.73 for Al. This difference in the clogging rate can also be seen in the AFM side profiles of the representative tapered structures ( $W/L=0.3$   $\mu\text{m} / 2$   $\mu\text{m}$ ) shown in Figure 3. This analysis reveals that Au clogs apertures slower than Al, allowing for more material accumulation for a given amount of deposited material. Because the clogging is initiated by the diffusion-driven grain growth into the aperture openings on the stencil membrane, the difference in the average grain size of the two metals (Al is coarser than Au), which can also be observed in the SEM and AFM images throughout this report, can be attributed to the difference in the clogging rate. In a recent report, metal grain size in evaporated films was studied and related to the deposition conditions, such as substrate temperature, deposition rate and vacuum conditions.<sup>28</sup> Therefore, the metal evaporation rules

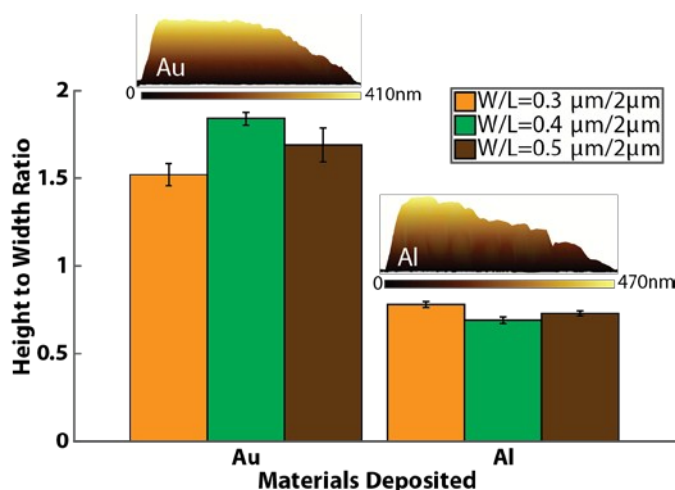


**Figure 3.** HtoW ratio collected statistically on tapered structures with three different W/L ratios and for two different materials (Al and Au) showing significant material effect on the HtoW ratio and as significant geometry dependence. Error bars represent the standard error over 12 samples for each tapered geometry.

disclosed in the literature<sup>28</sup> together with our proposed technique can be utilized as a toolbox to control the deposited metal film grain structures, and thus, the 3D metal nanostructure topographies. On the other hand, Köbel et al. has shown that stencil aperture clogging rate can be controlled by surface-modifying the stencil membrane exterior,<sup>29</sup> which can also be employed to slow down the aperture clogging rate, and therefore, forge high aspect-ratio structures.

Our method is highly adaptable to a wide range of geometries and dimensions. In Figure 4, a four-pointed star structure is shown in two different dimensions (with total widths 0.8  $\mu\text{m}$  and 1.4  $\mu\text{m}$ ) and materials (Al and Au). We observed that the smaller Al structure has a 3D geometry with a pointy center (max height=335 nm) formed as a result of the full closure of the aperture. For the same geometry, the Au structure is taller (410 nm) but has a flat top, which indicates that the total amount of metal deposited ( $\sim 400$  nm) was not enough to fully clog the stencil aperture. This agrees well with our earlier clogging rate comparison between Au and Al, and exemplifies our method's flexibility in 3D topographical manipulation of submicron structures using tuning parameters, such as aperture geometry and dimension; as well as material and deposition conditions.

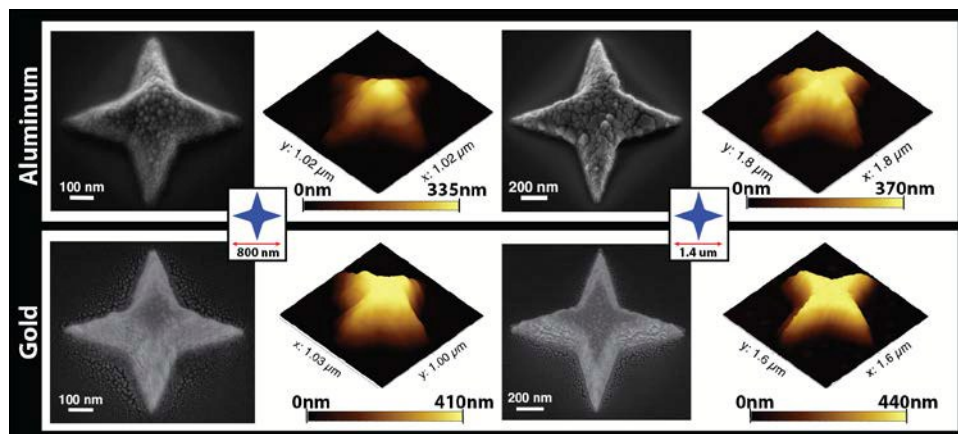


**Figure 4.** Scalability of the height control on a symmetric four-pointed star shape. Top and bottom rows show both the SEM images and the AFM topography of four-pointed star shapes for Al and Au materials, respectively. The pattern is presented in two dimension scales: smaller pattern on the left with 800 nm and bigger pattern on the right with 1.4  $\mu\text{m}$  total width. The average grain size of the Al and Au can be compared on the SEM micrographs.

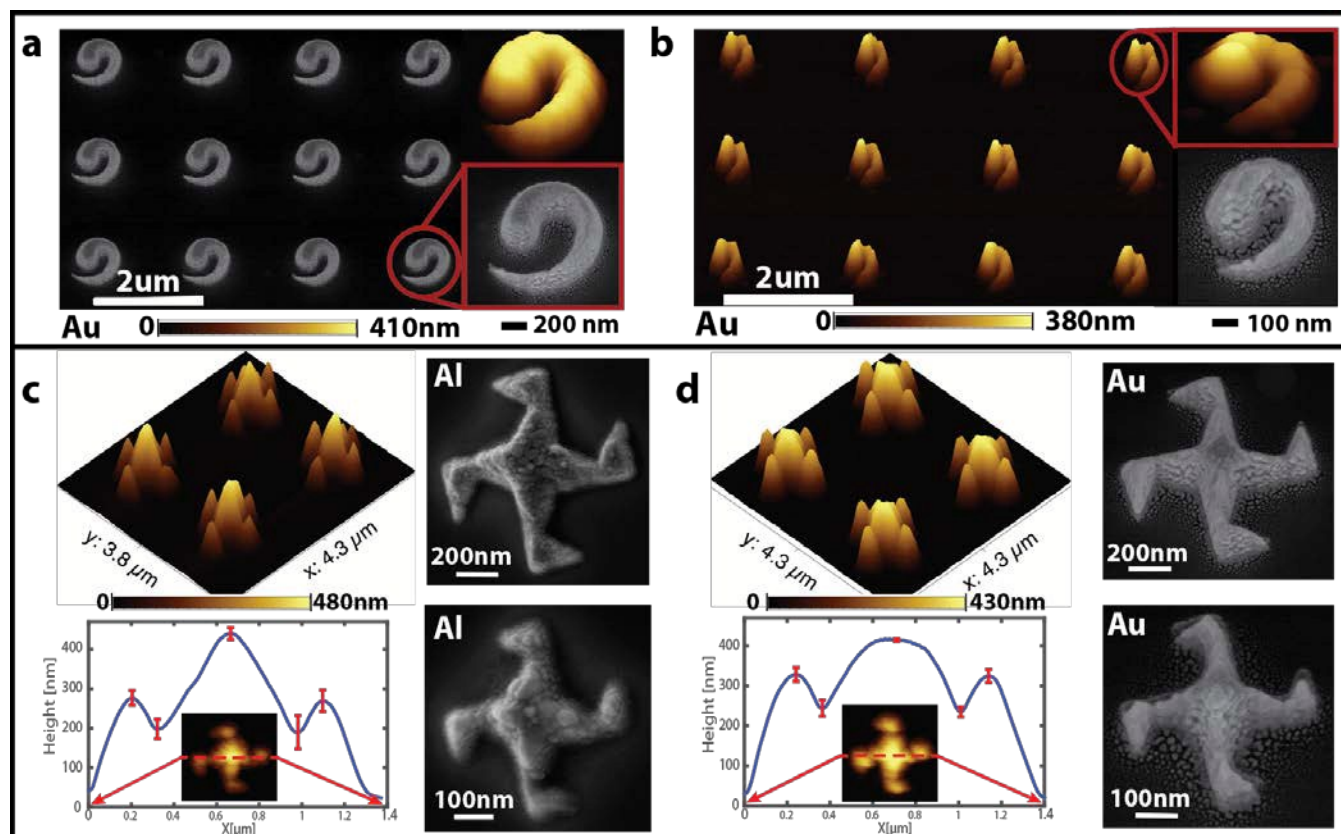


**Figure 5.** Arrayed 3D nanostructures created using the stencil clogging effect. Two different geometries are presented: snail structure (a, b) with curved features and windmill structure (c, d) with multi-peaks. Au snail structure arrays are presented in two dimensions: a) 1  $\mu\text{m}$  and b) 0.5  $\mu\text{m}$  total width and 2  $\mu\text{m}$  pitch in tilted ( $20^\circ$ ) SEM and AFM images. Resolution limiting blurring can be seen in the SEM micrographs. Windmill structure is shown in two different materials: c) Al and d) Au. The SEM images demonstrate the identical geometries in two dimension scales: 1  $\mu\text{m}$  (top) and 0.5  $\mu\text{m}$  (bottom) total structure width. 3D AFM topography images show a 2 X 2 portion of a 4 X 4 array. The plots show the average profiles extracted from the lateral axis of 12 structures. Error bars represent the standard deviation at the peak and the valley points.

We advance the discussion on the ability to control individual nanostructure topographies using stencil lithography by exploring asymmetric and irregular patterns, which is relevant for the fabrication of 3D structures that exhibit chirality. We first explored a curved geometry, which we call “snail structure.” A similar version of this structure, fabricated using hole-mask lithography in a randomly distributed manner, was optically characterized by Frank et al. and its distinct chiral properties were disclosed.<sup>22</sup> Figure 5 a and b show Au snail structures in two different sizes, with total widths 1  $\mu\text{m}$  and 0.5  $\mu\text{m}$ , respectively. Both the AFM and the SEM images of the arrayed (original array size = 4 X 4) snail structures show excellent homogeneity within the array. Second, we fabricated a pattern with irregular aperture width, which we call “windmill structure”, as seen in Figure 5 c and d in Al and Au,

respectively. The two by two arrays of the windmill structures (original array size = 4 X 4) presented using AFM data reveal that this method allows for the multi-peak, inhomogeneous height variation on individual structures in the sub-micron scale. Moreover, the SEM images of both the Al and Au single windmill structures with total widths of 1  $\mu\text{m}$  and 0.5  $\mu\text{m}$  show that this multi-peak 3D formation is scalable, with grain size and blurring being the dominant resolution restricting aspects. Blurring, the spreading of materials into the shadowed regions of the substrate, occurs because of substrate material diffusion and divergence of the materials reaching the substrate due to the gap between the stencil mask and the substrate.<sup>24</sup> Although we did not employ a corrective method in this work, it is important to point out that post-deposition corrective etching,<sup>30</sup> which removes a thin layer of unwanted

material without damaging the main structure, can be applied to improve the resolution in our method.

Furthermore, we analysed the topographical profiles extracted from the AFM scan data along the center horizontal axis of the windmill structures to comment on the topographical homogeneity. The averages of twelve profiles collected from different windmill structures in the same array are presented in Figure 5c and d for Al and Au, respectively, with the standard deviations indicated at the peak and the valley points. Since the variation in the 3D profiles stems primarily from the metal grain positions, standard deviations are larger with Al (average profile SD = 32 nm) than with Au (average profile SD = 16 nm) due to the larger average grain size of Al.

We presented a novel use of stencil lithography to extend its applications to height profile regulation that allows for the fabrication of 3D nanostructures with inhomogeneous thickness profiles. SEM and AFM acquired visual and topographical data is used to characterize the lithographic capabilities of our method. First, we quantified the clogging rate on various tapered line patterns by relating their AFM measured maximum height profiles to aperture widths and extracted HtoW ratios as 1.69 for Au and 0.73 for Al. Our analysis on the AFM data showed no significant influence of aperture dimension or geometry on the clogging rate; however, data revealed a strong material dependence. Moreover, we presented various patterns both with straight — four-pointed star and windmill— and curved —snail— geometric elements at different dimension scales, both with micron and submicron features, to illustrate the versatility and scalability of this approach, while discussing the resolution limiting aspects such as blurring and grain size dependence. Comparing individual windmill nanostructure profiles in an array, we were able to assess the homogeneity. The average profile standard deviation of arrayed windmill structures were measured as 32 nm and 16 nm for Al and Au, respectively, which is affected by the average grain size of each material. This novel application of stencil lithography for the third dimension control in the nanoscale has great potential to pave the way for applications in many fields, such as photonics and bio-inspired materials.

## Acknowledgements

This research is partially supported by the European Commission funded NanoVista Project (FP7-ICT-2011-7, under grant agreement No 288263) and EUJO-LIMMS Project (no. 295089).

## References

- 1 E. Hendry, T. Carpy, J. Johnston, M. Popland, R. V. Mikhaylovskiy, A. J. Laphorn, S. M. Kelly, L. D. Barron, N. Gadegaard and M. Kadodwala, *Nat. Nanotechnol.*, 2010, **5**, 783–787.
- 2 R. Tullius, A. S. Karimullah, M. Rodier, B. Fitzpatrick, N. Gadegaard, L. D. Barron, V. M. Rotello, G. Cooke, A. Laphorn and M. Kadodwala, *J. Am. Chem. Soc.*, 2015, **137**, 8380–8383.

- 3 X. Yin, M. Schäferling, A.-K. U. Michel, A. Tittl, M. Wuttig, T. Taubner and H. Giessen, *Nano Lett.*, 2015, **15**, 4255–4260.
- 4 S. Zhang, J. Zhou, Y.-S. Park, J. Rho, R. Singh, S. Nam, A. K. Azad, H.-T. Chen, X. Yin, A. J. Taylor and X. Zhang, *Nat. Commun.*, 2012, **3**, 942.
- 5 Y. Zhao, M. A. Belkin and A. Alù, *Nat. Commun.*, 2012, **3**, 870.
- 6 N. A. Cinel, S. Bütün, G. Ertaş and E. Özbay, *Small*, 2013, **9**, 531–537.
- 7 K. Jung, J. Hahn, S. In, Y. Bae, H. Lee, P. V. Pikhitsa, K. Ahn, K. Ha, J.-K. Lee, N. Park and M. Choi, *Adv. Mater.*, 2014, **26**, 5924–5929.
- 8 J. Y. Suh, M. D. Huntington, C. H. Kim, W. Zhou, M. R. Wasielewski and T. W. Odom, *Nano Lett.*, 2012, **12**, 269–274.
- 9 T. Darmanin and F. Guittard, *Mater. Today*, 2015, **18**, 273–285.
- 10 D. Tulli, S. D. Hart, P. Mazumder, A. Carrilero, L. Tian, K. W. Koch, R. Yongsunthon, G. A. Piech and V. Pruneri, *ACS Appl. Mater. Interfaces*, 2014, **6**, 11198–11203.
- 11 K.-C. Park, H. J. Choi, C.-H. Chang, R. E. Cohen, G. H. McKinley and G. Barbastathis, *ACS Nano*, 2012, **6**, 3789–3799.
- 12 S. Pogodin, J. Hasan, V. A. Baulin, H. K. Webb, V. K. Truong, T. H. Phong Nguyen, V. Boshkovikj, C. J. Fluke, G. S. Watson, J. A. Watson, R. J. Crawford and E. P. Ivanova, *Biophys. J.*, 2013, **104**, 835–840.
- 13 M. Hentschel, M. Schäferling, T. Weiss, N. Liu and H. Giessen, *Nano Lett.*, 2012, **12**, 2542–2547.
- 14 I. Staude, M. Decker, M. J. Ventura, C. Jagadish, D. N. Neshev, M. Gu and Y. S. Kivshar, *Adv. Mater.*, 2013, **25**, 1260–1264.
- 15 A. Radke, T. Gissibl, T. Klotzbücher, P. V. Braun and H. Giessen, *Adv. Mater.*, 2011, **23**, 3018–3021.
- 16 M. Esposito, V. Tasco, M. Cuscunà, F. Todisco, A. Benedetti, I. Tarantini, M. D. Giorgi, D. Sanvitto and A. Passaseo, *ACS Photonics*, 2015, **2**, 105–114.
- 17 J. Jeon, H. C. Floresca and M. J. Kim, *J. Vac. Sci. Technol. B*, 2010, **28**, 549–553.
- 18 X. Lan, X. Lu, C. Shen, Y. Ke, W. Ni and Q. Wang, *J. Am. Chem. Soc.*, 2015, **137**, 457–462.
- 19 S. J. Tan, M. J. Campolongo, D. Luo and W. Cheng, *Nat. Nanotechnol.*, 2011, **6**, 268–276.
- 20 M. Mastrangeli, *Micro- Nanoelectromechanical Syst.*, 2015, **6**.
- 21 X. A. Zhang, B. Dai, Z. Xu and C.-H. Chang, *Small*, 2015, **11**, 1226–1226.
- 22 B. Frank, X. Yin, M. Schäferling, J. Zhao, S. M. Hein, P. V. Braun and H. Giessen, *ACS Nano*, 2013, **7**, 6321–6329.
- 23 R. Walter, A. Tittl, A. Berrier, F. Sterl, T. Weiss and H. Giessen, *Adv. Opt. Mater.*, 2015, **3**, 398–403.
- 24 O. Vazquez-Mena, L. Gross, S. Xie, L. G. Villanueva and J. Brugger, *Microelectron. Eng.*, 2015, **132**, 236–254.
- 25 O. Vázquez-Mena, G. Villanueva, M. A. F. van den Boogaart, V. Savu and J. Brugger, *Microelectron. Eng.*, 2008, **85**, 1237–1240.
- 26 V. Flauraud, T. S. van Zanten, M. Mivelle, C. Manzo, M. F. Garcia Parajo and J. Brugger, *Nano Lett.*, 2015, **15**, 4176–4182.
- 27 O. Vazquez-Mena, G. Villanueva, V. Savu, K. Sidler, M. A. F. van den Boogaart and J. Brugger, *Nano Lett.*, 2008, **8**, 3675–3682.
- 28 K. M. McPeak, S. V. Jayanti, S. J. P. Kress, S. Meyer, S. Iotti, A. Rossinelli and D. J. Norris, *ACS Photonics*, 2015, **2**, 326–333.
- 29 M. Kölbl, R. W. Tjerkstra, J. Brugger, C. J. M. van Rijn, W. Nijdam, J. Huskens and D. N. Reinhoudt, *Nano Lett.*, 2002, **2**, 1339–1343.
- 30 J. Arcamone, A. Sánchez-Amores, J. Montserrat, M. A. F. van den Boogaart, J. Brugger and F. Pérez-Murano, *J. MicroNanolithography MEMS MOEMS*, 2007, **6**, 013005–013005–7.